Volume 9
Number 26
14 July 2021
Pages 5165–5376

Journal of Materials Chemistry B

Materials for biology and medicine

rsc.li/materials-b

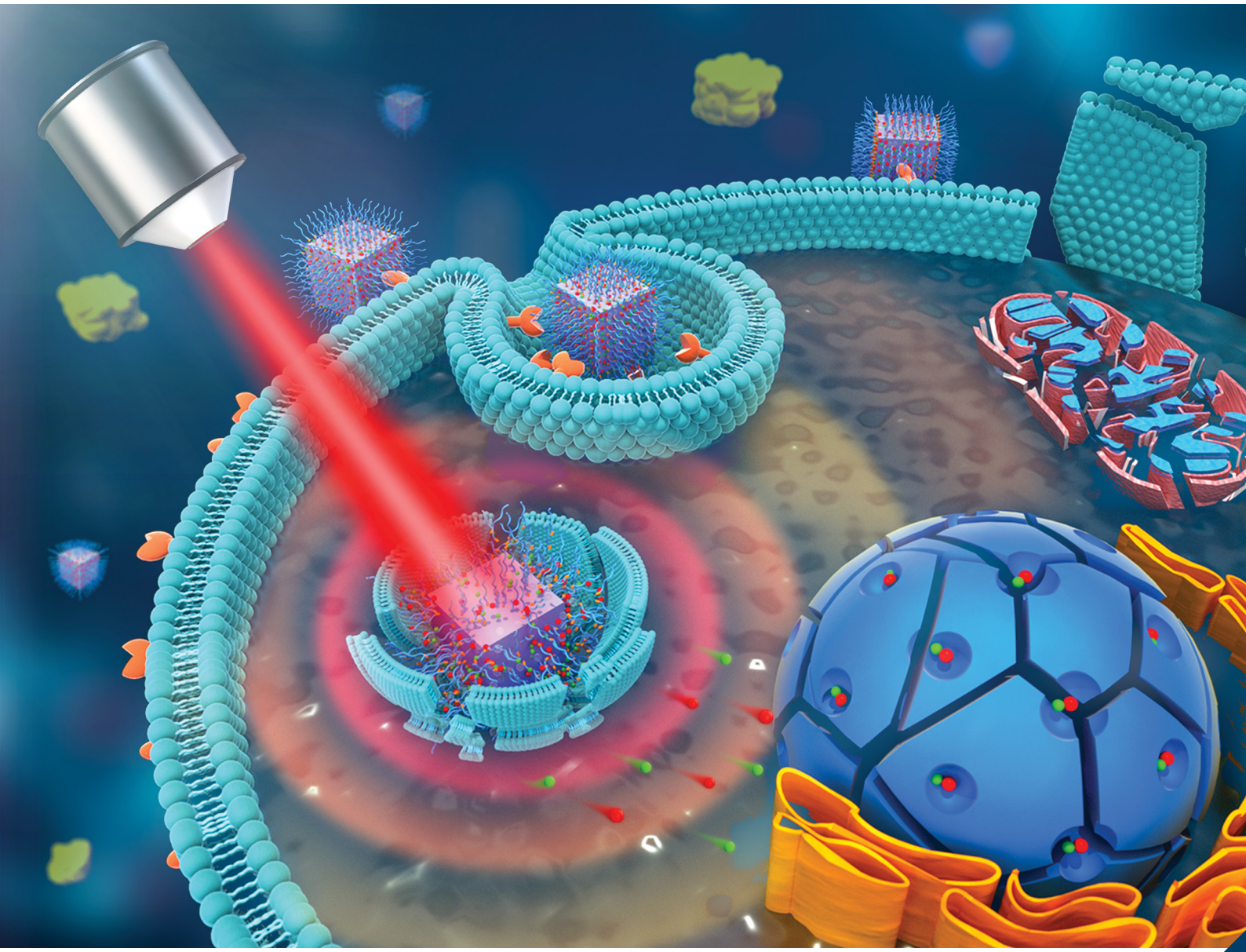

ISSN 2050-750X

ROYAL SOCIETY OF CHEMISTRY

PAPER

Haiyan Xu, Ning Gu, Yu Zhang *et al.*
Zwitterion-functionalized hollow mesoporous Prussian blue nanoparticles for targeted and synergetic chemo-photothermal treatment of acute myeloid leukemia

Indexed in Medline!

Journal of Materials Chemistry B

ROYAL SOCIETY OF CHEMISTRY

PAPER

View Article Online
View Journal | View Issue

Cite this: *J. Mater. Chem. B*, 2021, **9**, 5245

Zwitterion-functionalized hollow mesoporous Prussian blue nanoparticles for targeted and synergetic chemo-photothermal treatment of acute myeloid leukemia†

Huiyuan Bai,[a] Quanhao Sun,[a] Fei Kong,[a] Haijiao Dong,[a] Ming Ma,[a] Fangzhou Liu,[c] Chen Wang,[d] Haiyan Xu,*[b] Ning Gu*[a] and Yu Zhang*[a]

Received 13th March 2021,
Accepted 20th May 2021

DOI: 10.1039/d1tb00548k

rsc.li/materials-b

Multifunctional drug delivery systems combining two or more therapies have a wide-range of potential for high efficacy tumor treatment. Herein, we designed a novel hollow mesoporous Prussian blue nanoparticles (HMPBs)-based platform for targeted and synergetic chemo-photothermal treatment of acute myeloid leukemia (AML). The HMPBs were first loaded with the anticancer drugs daunorubicin (DNR) and cytarabine (AraC), and were subsequently coated with polyethylenimine (PEI) through electrostatic adsorption. Then, zwitterionic sulfobetaine (ZS) and CXCR4 antagonist peptide E5 were modified onto the surface of the nanoparticles *via* covalent bonding to fabricate a nanoplatform (denoted as HMPBs(DNR + AraC)@PEI-ZS-E5). The nanoplatform showed excellent photothermal effects, superior photothermal stability, reduced nonspecific protein adsorption, efficient targeting capability, a constant hydrodynamic diameter and good biocompatibility. Additionally, a laser-responsive drug release pattern was observed. *In vitro* results indicated that the nanoplatform could achieve active targeting and remarkable chemo-photothermal synergetic therapeutic effects, showcasing its great potential in AML treatment.

1. Introduction

Acute myeloid leukemia (AML) is a highly lethal disease, which seriously endangers human health.[1,2] Currently, chemotherapy is the most widely used treatment for AML. However, treatment is still far from optimal therapeutic efficacy due to poor bioavailability, nonspecific organ toxicity and the high possibility of recurrence.[3–5]

In recent years, combinational strategies based on nanomaterials have shown to have promising potential for improving the curative effects for cancer.[6–8] As a non-invasive therapeutic strategy, photothermal therapy has generated increasing interest due to its great advantages such as safety, high efficiency, broad-spectrum and minimal side effects in healthy tissues.[9–13] Photothermal therapy employs photoabsorbers to convert the photon energy into heat using near-infrared region (NIR) light irradiation in order to destroy tumor cells.[14,15] At present, diverse nanostructures have been exploited to achieve the desirable treatment efficacy for tumor ablation, including noble metal nanoparticles, carbon-based nanostructures, iron-based magnetic nanoparticles, organic substance-like indocyanine green, and so on.[16–21] Prussian blue (PB) has shown strong absorption in the NIR region, high photothermal conversion efficiency, and good photothermal stability.[22–24] Furthermore, due to its outstanding biocompatibility, PB has been approved by the USA Food and Drug Administration as an antidote for radioactive exposure.[25–27] All these excellent properties contribute to the PB-based nanostructure being an ideal photothermal agent for photothermal therapy.

Improving drug accumulation in the tumor and reducing the side effects of chemotherapeutics in normal tissues are important research aspects in tumor therapy. Improving the treatment efficiency and changing the pharmacokinetics is one of the main focuses of the research. To date, various antifouling materials such as ethylene glycol-based polymers and oligomers have been employed to achieve long blood circulation and better

[a] *State Key Laboratory of Bioelectronics, Jiangsu Key Laboratory for Biomaterials and Devices, School of Biological Science and Medical Engineering and Collaborative, Innovation Center of Suzhou Nano Science and Technology, Southeast University, Nanjing 210096, P. R. China. E-mail: zhangyu@seu.edu.cn, guning@seu.edu.cn*

[b] *Institute of Basic Medical Sciences, Chinese Academy of Medical Sciences & Peking Union Medical College, Beijing 100005, P. R. China. E-mail: xuhy@pumc.edu.cn*

[c] *Department of Head & Neck Surgery, Jiangsu Cancer Hospital & Jiangsu Institute of Cancer Research, The Affiliated Cancer Hospital of Nanjing Medical University, Nanjing 210029, P. R. China*

[d] *National Center for Nanoscience and Technology, Beijing 100190, P. R. China*

† Electronic supplementary information (ESI) available. See DOI: 10.1039/d1tb00548k

treatment efficiency. It is well known that PEGylation is widely used in surface chemistry to optimize the *in vivo* pharmacokinetics of nanoparticles. Unfortunately, PEG-based ligand modified nanoparticles tend to aggregate in high-salinity buffers. In addition, the PEG polymer can increase the hydrodynamic diameter of the nanoparticles, which limits their access to confined spaces and prevents their renal elimination.[28,29] Zwitterionic polymers containing equal numbers of cationic and anionic groups have generated great attention in the biomedical field. Sulfobetaine, a typical representative among zwitterionic polymers, shows excellent resistance to nonspecific interactions with proteins because of its superior hydrated property and near neutral surface charge.[30,31] Zwitterion modifications have endowed the nanoparticles with a small hydrodynamic size, prolonged blood circulation time and a minimal immune response. In addition, using targeting groups to modify the nanomaterials in order to enhance their targeting ability can also achieve effective drug accumulation at the desired sites and improve the treatment efficiency.[32–36] The C–X–C chemokine receptor type 4 (CXCR4) is considered an important target in AML therapy, and is related to AML relapse. Generally, high levels of CXCR4 on leukemia cells can interact with chemokine ligand 12, which is secreted by bone marrow stroma cells to obtain anti-apoptosis signals for survival.[37–40] Hence, CXCR4 plays an important role in AML treatment.

Based on the above, we have designed and synthesized a new drug delivery system for targeted and synergetic chemo-photothermal treatment of AML. As shown in Scheme 1, multifunctional and well-dispersed hollow mesoporous Prussian blue nanoparticles (HMPBs) were synthetized using a facile method, providing a large surface area for drug loading. After loading with daunorubicin (DNR) and cytarabine (AraC), polyetherimide (PEI) was attached onto the surface. Then, the ZS ligand produced by radical copolymerization of acrylic acid (AA) and [2-(methacryloyloxy)ethyl] dimethyl-(3-sulfopropyl)ammonium hydroxide (DMAPS), was further coated around the surface of the nanoparticles. It is expected that the combination of a quaternary amine group and the sulfonate group could provide the ligand with zwitterionic character and minimal nonspecific protein adsorption. E5 is a novel peptide with high affinity towards CXCR4 overexpressed leukemia cells. Meanwhile, compared with other CXCR4 antagonists (*e.g.* chemical molecules and antibodies), E5 exhibits superior advantages including low price, safety and an easy synthesis.[41,42] Thus, the CXCR4 antagonist peptide E5 was attached onto the surfaces of nanoparticles to obtain HMPBs(DNR + AraC)@PEI-ZS-E5, with an aim to endow the PBNPs with a specific targeting ability for leukemia cells. *In vitro* studies demonstrated the excellent properties of HMPBs(DNR + AraC)@PEI-ZS-E5 in AML treatment: excellent biocompatibility, high drug loading, anti-protein adsorption property, laser-triggered drug release profile, active targeting capability, and good chemo-photothermal synergistic therapeutic effects.

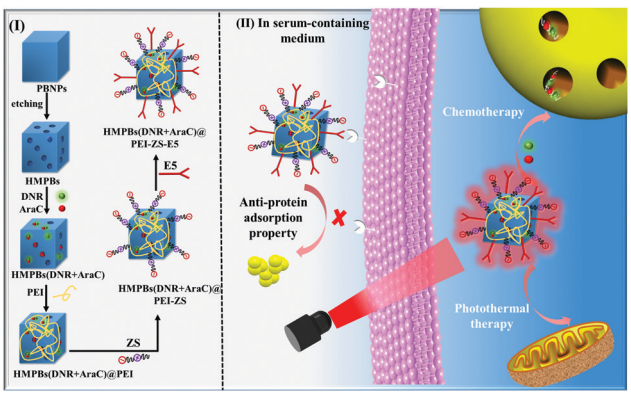

Scheme 1 (I) Schematic illustrations for the preparation of HMPBs(DNR + AraC)@PEI-ZS-E5. (II) Schematic illustrations of HMPBs(DNR + AraC)@PEI-ZS-E5 for targeted and synergetic chemo-photothermal treatment of AML.

2. Experimental section

2.1 Materials

Polyvinylpyrrolidone (PVP, M_w = 30 kDa), potassium ferricyanide ($K_3Fe(CN)_6{\cdot}3H_2O$), and hydrochloric acid (HCl, 36.0–38.0%) were provided by the Guoyao Group Chemical Reagent Co. Ltd. DNR, AraC, 1-(3-dimethyl aminopropyl)-3-ethylcarbodiimide hydrochloride (EDC), PEI, DMAPS and AA were obtained from Sigma-Aldrich. The ammonium persulfate (APS) was supplied by Aladdin Chemistry Co. Ltd. E5 (GGRSFFLLRRIQGCRFRNTVDD) was synthesized by Guoping Pharmaceutical Co. Ltd. The deionized (DI) water was purifed using a Milli-Q gradient system.

2.2 Synthesis of ZS and HMPBs@PEI-ZS-E5

First, 36.6 mg of DMAPS and 4.24 mg of AA were dissolved in 100 mL DI water under magnetic stirring. After being stirred for 0.5 h, the copolymerization reaction was initiated by 40 mg of APS. The solution was purged with nitrogen for 0.5 h to remove oxygen and was then kept at 75 °C for 6 h with stirring under a nitrogen atmosphere. Finally, the mixture was dialyzed for 48 h using a dialysis bag (500 Da, MWCO) to remove the unreacted monomers. The obtained solution was stored at 4 °C for further use.

The HMPBs were prepared according to the previously published methods. First, 131.7 mg of $K_3[Fe(CN)_6]$ and 3 g of PVP were dissolved into 40 mL of HCl solution (0.01 M), and stirred for 0.5 h. The mixture was transferred into a three-neck bottle and heated in a water bath at 80 °C for 20 h. Afterwards, the PBNPs were obtained following centrifugation and being washed three times. Then, 20 mg of the PBNPs and 100 mg of PVP was added into 20 mL of HCl solution (1 M). After stirring for 1 h, the solution was transferred into a Teflon autoclave and heated in an electric oven at 140 °C for 3.5 h. The HMPBs were obtained after centrifugation and after being washed with DI water three times. The PEI-modified HMPBs (HMPBs@PEI) were prepared by the dropwise addition of 10 mL of PEI solution (0.2 mg mL^{-1}) to 10 mL of HMPBs dispersion (0.5 mg mL^{-1}) and stirring for 1 h at room temperature. The products were purified three times using ultrafiltration (100 kDa, MWCO) and then stored at 4 °C. To synthesize

HMPBs@PEI-ZS, 2 mL of ZS solution (0.5 mg mL^{-1}) was mixed with 200 μL of EDC (10 mg mL^{-1}), in order to activate the carboxyl, for 2 h. Then, dropwise addition of an activated ZS solution into 10 mL of a HMPBs@PEI dispersion (0.5 mg mL^{-1}) was carried out and was stirred for 12 h. After purifying three times using ultrafiltration (100 kDa, MWCO), the products were stored at 4 °C for future experiments. To synthesize HMPBs@PEI-ZS-E5, 200 μL of the E5 solution (1 mg mL^{-1}) was mixed with 200 μL EDC (10 mg mL^{-1}) for 2 h. Then, the mixture was added into 10 mL of the prepared HMPBs@PEI-ZS (0.5 mg mL^{-1}) and stirred for 12 h at 4 °C. HMPBs@PEI-ZS-E5 were obtained after purification using ultrafiltration (100 kDa, MWCO) and being washed with DI water three times. The E5 contents of HMPBs@PEI-ZS-E5 were measured using a BCA protein assay kit.

2.3 Characterizations

Transmission electron microscopy (TEM, JEOL, Japan) were used to characterize the morphology and particle sizes of the nanoparticles. The particle size, polymer dispersity index (PDI) and zeta potential were examined using dynamic light scattering (DLS, Malvern Zetasizer, UK). The UV-vis absorption spectra were obtained using a UV–vis spectrophotometer (UV-3600, Shimadzu, Japan). Fourier transform infrared (FT-IR) spectra were acquired using an FTIR-FTS3000 spectrometer. The crystalline form was characterized using an X-ray diffractometer with a powder sample (X'TRA, Switzerland). Fluorescence spectroscopy of the as-synthesized nanoparticles was performed with a Horiba Fluoromax-4 spectrofluorophotometer. Pore size was measured on a Tristar II 3020 physisorption system (Micromeritics Instrument Corporation, USA).

2.4 Photothermal effect study

To study the photothermal effect, HMPBs@PEI-ZS-E5 at different concentrations were added into transparent quartz cells. DI water was set as a control. The solutions were irradiated with an 808 nm laser with a power density of 1.5 or 2 W cm^{-2}. The temperature of the solution was recorded. In addition, a thermal infrared imaging camera (Fluke, USA) was used to monitor the temperature. Then, the HMPBs@PEI-ZS-E5 solution was irradiated with a laser for 5 min and was then cooled down. The temperature change was recorded during the repeated five cycles. In addition, the UV-vis absorbance spectra of HMPBs@PEI-ZS-E5 before and after irradiation were also recorded.

2.5 Drug loading and release study

To prepare the drug loaded nanoparticles, both DNR and AraC (0.2 mg mL^{-1}) were added dropwise into appropriate HMPB solutions. After stirring for 24 h in the dark, the nanoparticles were centrifuged and the supernatant was collected. The obtained nanoparticles were then functionalized with PEI, ZS, and E5 using similar methods as mentioned in the "preparation of HMPBs@PEI-ZS-E5" section. The unbound drug in the supernatant was analyzed using a UV–vis spectrophotometer at 480 nm for DNR and at 272 nm for AraC, based on a standard curve (absorbance intensity *versus* concentration). The drug loading content (LC) and encapsulation efficiency (EE) were calculated by the following equation: LC = (total drug − unencapsulated drug)/total drug loaded HMPBs × 100%

EE = (total drug − unencapsulated drug)/total drug × 100%

To evaluate the drug release behavior, 10 mL of the drug loaded samples with appropriate concentrations were placed into dialysis bags (10 kDa, MWCO). Then, the suspension was immersed in PBS buffer. The released amount of drugs was monitored at regular time intervals. To examine the laser-induced drug release behavior, the dialysis bag was exposed to a laser (2 W cm^{-2}) for four on/off cycles (laser on: 5 min, laser off: 10 min). All the samples were stirred at 100 rpm. Then, 1 mL of the solution was taken out at desired time points and replaced with an equal volume of fresh buffer. The concentration of the released drug was measured using a UV–vis spectrophotometer and calculated according to the standard curve.

2.6 Protein adsorption and biosafety evaluation

The protein adsorption capability was investigated by suspending the nanoparticles in tubes containing bovine serum albumin (BSA). Briefly, the nanoparticles (0.1 mg mL^{-1}) and BSA (0.2 mg mL^{-1}) were mixed in a 1 : 1 volume ratio. After incubation for 1, 2, and 4 h at 37 °C under shaking, the suspensions were centrifuged. The content of the unbound protein in supernatant was measured using a BCA protein assay kit. The percentage of adsorbed protein was analyzed by the mass ratio of the adsorbed protein to the total protein. In addition, HMPBs@PEI-ZS-E5 were incubated in PBS with 10% FBS and preserved in the dark for 48 h at room temperature. The hydrodynamic size of HMPBs@PEI-ZS-E5 was detected at different time points. In order to investigate the biosafety, HL60 cells (1×10^5 cells per well) were seeded in 96-well plates. Then, HMPBs, HMPBs@PEI-ZS and HMPBs@PEI-ZS-E5 with a concentration ranging from 10 to 100 μg mL^{-1} were added into the well and cultured for 24 h. Then, 10 μL of CCK-8 (Keygen, China) was added into the medium and cultured for another 4 h. The absorbance at 450 nm was recorded using a Multi-Mode Microplate Reader. To test the hemolysis effect, erythrocytes were collected after removing the serum by centrifugation. After washing with PBS three times, PBS was mixed with erythrocytes in a 9 : 1 volume ratio. Then, nanoparticles at varying concentrations were added and incubated for 6 h. Erythrocytes incubated with DI water were employed as a control. Following this, the supernatants were collected by centrifugation. The hemoglobin contents were detected by measuring the absorbance at 540 nm. The hemolysis ratio was calculated by the following equation:

$$\text{Hemolysis (\%)} = (A/A_0) \times 100\%$$

A and A_0 are the absorbance of the supernatants for the erythrocyte mixed with the nanoparticles and DI water, respectively.

2.7 Cellular uptake study

Flow cytometry and confocal fluorescence microscopy were used to evaluate cellular uptake. HL60 cells (2×10^6 cells per well)

were seeded in 6 well-plates. Then, the free drug, HMPBs(DNR + AraC), HMPBs(DNR + AraC)@PEI-ZS and HMPBs(DNR + AraC)@PEI-ZS-E5 at a DNR concentration of 5 μM were added to the culture medium for 4 h of incubation. In the inhibition experiment, 5 μM of E5 was cultured with cells for 1 h prior to nanoparticle uptake. Subsequently, the cells were rinsed and washed with PBS, resuspended in cold PBS and analyzed with flow cytometry (FACS Calibuar, USA) by detecting DNR fluorescence signals. For visualized observation, cells were washed and placed in a cytospin on a slide at 1500 rpm for 10 min. Then, these cells were stained with Hoechst 33342 (Beyotime, China) for 10 min. Images were captured using confocal laser scanning microscopy (CLSM).

We further used ICP-OES to investigate cellular uptake. HL60 cells (2×10^6 cells per well) were seeded in 6 well-plates. Then, different HMPBs at the same concentration of 100 μg mL^{-1} were added into the culture medium. To block the receptors, 5 μM of E5 was cultured with cells for 1 h prior to nanoparticle uptake. After 24 h incubation, the HL60 cells were washed, harvested and counted. The "Fe" content was measured after lysing the cells with aqua regia.

2.8 CCK-8 assay

HL60 cells (1×10^5 cells per well) were seeded in 96-well plates. Then, different HMPBs with the same concentration ranging from 10 to 50 μg mL^{-1} were added into the wells and cultured for 4 h. After that, the cells were irradiated using an 808 nm laser (1.5 W cm^{-2}) for 5 min in the irradiation group. After being cultured for 20 h, 10 μL of CCK-8 was added into the culture medium and then cultured for another 4 h. The absorbance at 450 nm was recorded by a Multi-Mode Microplate Reader.

2.9 Cell apoptosis assay

Annexin V-APC/7-AAD staining was used to detect the apoptosis of HL60 cells. Briefly, different HMPBs with the same concentration of 10 μg mL^{-1} were added into the wells and cultured for 4 h. Then, the cells were irradiated with a laser (1.5 W cm^{-2}) for 5 min in the irradiation group. The HL60 cells without any treatment were set as a control. The cells were collected, washed and resuspended in the binding buffer after being cultured for 20 h. Annexin V-APC and 7-AAD (Keygen, China) were added and incubated for 10 min in the dark. Finally, the cells were subjected to flow cytometry and the acquired data was analyzed using FlowJo 7.6.

2.10 Live/dead cell staining

HL60 cells (2×10^6 cells per well) were seeded in 6 well-plates. Then, different HMPBs with the same concentration of 50 μg mL^{-1} were added into the wells (2×10^6 cells per well) and cultured for 4 h. Then, the cells were irradiated using a laser (1.5 W cm^{-2}) for 5 min. The HL60 cells without any treatment were set as a control. After being cultured for 20 h, the cells were rinsed and stained with 2 μM calcein-AM (Keygen, China) and 8 μM PI (Keygen, China) for 45 minutes. Then, the cells were imaged using a fluorescence microscope.

2.11 Measurement of mitochondrial membrane potential (MMP) and ROS

The treatment of the HL60 cells is the same as in the "Live/dead cell staining" section. The HL60 cells were collected and stained with JC-1 solution for 20 min in the dark. Then, the cells were washed and imaged using a fluorescence microscope.

For ROS detection, HL60 cells were incubated with 50 μg mL^{-1} HMPBs@PEI-ZS-E5 for 4 h. Then, the cells were treated with or without laser irradiation (1.5 W cm^{-2}) for 5 min. After incubation for 20 h, DCFH-DA (10 μM) was added and incubated at 37 °C for 20 min. Then, the cells were washed, collected and detected by a spectrofluorophotometer.

2.12 Phospho-histone H2AX detection and quantitative reverse transcription-polymerase chain reaction (qRT-PCR) analysis

The treatment of the HL60 cells is the same as in the "Live/dead cell staining" section. The HL60 cells were rinsed and centrifuged at 300 g for 5 min. Then, the supernatant was discarded and pre-cooled 70% ethanol was added dropwise. After incubation at −20 °C for 60 minutes, the cells were washed and resuspended in 100 μL PBS. Then, 5 μL of an FITC anti-H2AX phosphor (Ser139) antibody (BioLegend, USA) was added and stained for 1 h in the dark. The cells were washed twice and were detected using flow cytometry.

For the qRT-PCR assay, the total RNA of the HL60 cells was extracted using TRIzol® reagent (Invitrogen, USA). Then, the RNA was reverse-transcribed into cDNA using a High-Capacity cDNA Reverse Transcription kit (Applied Biosystems, USA). RT-qPCR analyses were performed using a SYBR green qPCR Master Mix kit (Takara, Japan) on a Roche Real-Time PCR system (Roche, Germany). The PCR thermocycler conditions were as follows: 95 °C for 10 min, followed by 40 cycles of amplification at 95 °C for 15 s and 60 °C for 30 s. Glyceraldehyde-3-phosphate dehydrogenase (GAPDH) was used as the internal control. Table S1 (ESI†) presents the sequences of the primers employed. Each experiment was repeated three times. Finally, the $2^{-\Delta\Delta Ct}$ method was applied to determine gene expression.

2.13 Statistical analysis

Statistical calculations were performed in GraphPad Prism 7.0, and all values were presented as mean ± SD. Comparisons were conducted using one-way analysis of variance. Values of $^*p < 0.05$ and $^{**}p < 0.01$ were considered statistically significant.

3. Results and discussion

3.1 Synthesis and characterizations

The engineering procedure of HMPBs@PEI-ZS-E5 was prepared as follows. Briefly, PVP-coated Prussian blue nanoparticles were first prepared, followed by etching with HCl to obtain HMPBs. Then, PEI was adsorbed around the surface of the nanoparticles through electrostatic adsorption to endow the HMPBs with functional groups. On the other hand, PEI is one of the

typical lysosomal escape agents, which can promote lysosomal escape and increase drug release to maintain effective drug concentration. Subsequently, ZS synthesized by copolymerization is employed to endow HMPBs@PEI-ZS with an antifouling property. Finally, E5 was bonded onto the surface of the nanoparticles through an amide reaction to achieve the leukemia cell-targeting capability. The obtained HMPBs@PEI-ZS-E5 are well-dispersed with an average particle size of ~96 nm. PEI coating could not significantly influence the morphology of the HMPBs. After modification with ZS and E5, a thin layer was formed on the HMPBs (Fig. 1a).

The zeta potential and hydrodynamic diameter of the nanoparticles at different fabrication stages were measured. As shown in Fig. 1b and c, the zeta potential increased from about -16.8 ± 1.5 mV for HMPBs to 21.3 ± 1.2 mV for HMPBs@PEI, due to the attachment of positively charged PEI on the surface of HMPBs. The average hydrodynamic diameter was found to be 116.3 ± 0.5 nm for HMPBs and 125.6 ± 1.6 nm for HMPBs@PEI, indicating that the hydrodynamic size increased along with the assembly process. ZS is synthesized by free radical copolymerization of AA and DMAPS monomers in the presence of the cross-linker APS. The FT-IR spectrum showed characteristic absorption peaks at 1710 and 1415 cm^{-1}, which were assigned to the C=O stretching vibration and the O–H flexing vibration in AA, respectively. Furthermore, characteristic peaks at 1055 and 1014 cm^{-1} were assigned to the SO_3^- group in DMAPS. The above results suggest the successful preparation of ZS (Fig. S1, ESI†). After ZS is coated, the surface charge of the nanoparticles is near-electro neutrality (1.56 mV), which can be attributed to equal amounts of positive and negative charges of the passivating zwitterions on the surfaces of the HMPBs@PEI-ZS. Not surprisingly, the hydrodynamic diameter displayed a slight change between HMPBs@PEI and HMPBs@PEI-ZS (127.7 nm) when in aqueous medium. We deduced that the surface coating of the nanoparticles using zwitterion ligands may maintain the compact and small size of the nanoparticles, and this may enhance both the diffusivity and the EPR effect.[43] Upon E5 conjugation, the prepared HMPBs@PEI-ZS-E5 possessed a zeta potential of ~2.9 mV. The E5 conjugation rate is 75.3%, which was determined by BCA methods. Meanwhile, crystallography data was measured by X-ray diffraction (XRD) analysis. There are four major diffraction characteristic peaks at 17.3, 24.9, 35.0, and 39.6, which could be assigned to the (200), (220), (400), and (420) crystal planes of HMPBs, respectively (Fig. S2, ESI†).[44] These results confirmed that there is no significant change in the structure of the nanoparticles.

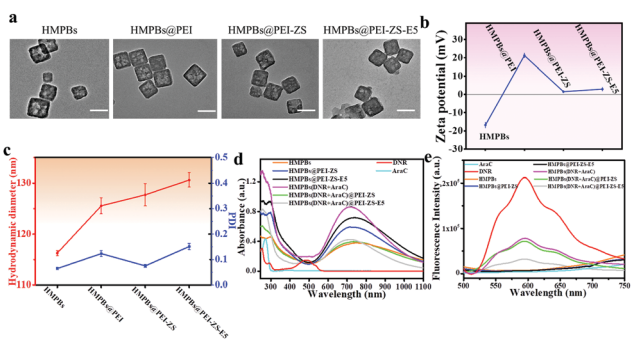

Fig. 1 Physicochemical property characterizations. (a) TEM images of different HMPBs. The scale bar is 100 nm. (b) Zeta potential and (c) hydrodynamic diameters of different HMPBs, measured by DLS at 25 °C. (d) UV-vis and (e) fluorescence spectra of AraC, DNR and different HMPBs.

3.2 Photothermal effect evaluation

The HMPBs@PEI-ZS-E5 exhibit a broad and strong NIR absorption band from around 600 to 900 nm, and this is essential for the NIR laser driven photothermal treatment application. To examine the calorigenic potential, HMPBs@PEI-ZS-E5 aqueous solutions were irradiated with an 808 nm laser for 5 min, respectively. The infrared thermographic maps showed that HMPBs@PEI-ZS-E5 displays good thermogenesis upon laser irradiation (Fig. 2a). Meanwhile, a clear concentration-dependent temperature increase was observed (Fig. 2b, c and Fig. S3, ESI†). The HMPBs@PEI-ZS-E5 showed high photothermal conversion capability and the photothermal conversion efficiency is calculated to be 39.6% (Fig. S4, ESI†). Importantly, HMPBs@PEI-ZS-E5 exhibited excellent photostability after laser irradiation and presented almost the same absorbance even after five cycles (Fig. 2d and e).

3.3 Drug loading and stimuli-responsive drug release pattern study

To realize the synergistic chemo-photothermal treatment, DNR and AraC were chosen as two model anticancer drugs for co-delivery to leukemia cells. By mixing both DNR and AraC with HMPBs, followed by a centrifugation process, HMPBs(DNR + AraC) were successfully synthesized. These drugs are encapsulated into HMPBs through coordinative bonding between inherent Fe in the structure of HMPBs and amino groups of the drugs. In addition, HMPBs with a mesoporous structure also contributed to the drug loading (Fig. S5, ESI†). The HMPBs (DNR + AraC)@PEI-ZS-E5 were obtained after functionalization with PEI, ZS and E5 ligands. The successful encapsulation of DNR and AraC into HMPBs was demonstrated by both UV–vis and fluorescence

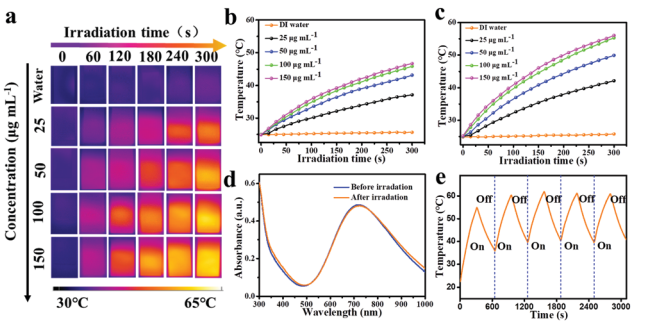

Fig. 2 Photothermal effect evaluation. (a) Infrared thermal images of the cuvettes containing HMPBs@PEI-ZS-E5 at various concentrations under laser irradiation for 5 min. Temperature elevations of HMPBs@PEI-ZS-E5 dispersion during laser irradiation for 5 min at a power density of (b) 1.5 and (c) 2 W cm^{-2}. (d) UV–vis spectra of HMPBs@PEI-ZS-E5 dispersion before and after laser irradiation. (e) Temperature variation of the HMPBs@PEI-ZS-E5 dispersion during cyclic laser exposure.

spectra. As shown in Fig. 1d, drug loaded nanoparticles showed UV–vis characteristic peaks of DNR and AraC at 480 nm and 272 nm, respectively. In addition, the DNR fluorescence peak at 585 nm also confirmed the successful loading of the drugs (Fig. 1e). The EE of DNR and AraC in HMPBs (DNR + AraC)@PEI-ZS-E5 was calculated to be 90.8% and 80.5%, respectively. The LC was determined to be 16.2% and 12.4%, for DNR and AraC, respectively (Table S2, ESI†). Compared to AraC, the increase of EE and LC for DNR was 10.3% and 3.8%, respectively, resulting from the different physicochemical properties of the drugs.[45,46]

The release behavior of the drugs from the different HMPBs was first evaluated under physiologic conditions. The cumulative release of DNR and AraC was only about 33.02–34.83% and 33.63–36.46% within 48 h (Fig. 3a and c), respectively, and this could be attributed to the slow exchange rate between the aqueous solution and the drug through the mesoporous structure. The controlled drug release profiles were further recorded under laser exposure. Rapid drug release in response to laser irradiation was observed (Fig. 3b and d). The release percentage increased to 52.85–54.13% for DNR and 45.61–49.13% for AraC within 70 min, respectively, providing evidence of laser-triggered drug release. It can likely be attributed to the high autologous photothermal effect of PB, resulting in accelerated drug diffusion and a rapid exchange rate between the internal space of the nanoparticles and the external solution environment.

3.4 Protein adsorption study and stability evaluation

More than half of the human blood is composed of plasma, which has a high concentration of proteins consisting of positively and negatively charged amino acids. When nanoparticles are introduced as foreign materials in the bloodstream, they tend to adsorb proteins by electrostatic, hydrophobic and hydrogen-bond interactions. Protein adsorption remains a challenge that hinders long circulation of the nanocarriers in the blood, by accelerating the clearance of nanoparticles by the mononuclear phagocyte system and leading to a serious inflammatory response. Zwitterions have been well-known essential adjuncts to such nanoparticulate therapies through two main attributes. Firstly, they endow nanoparticles with hydrophilicity, enhancing their ease of circulation and distribution in the bloodstream. Secondly, they impart nanoparticles with antifouling properties to prevent the formation of biomolecular coronas.[47–49] To examine the anti-protein adsorption capability of the nanoparticles, BSA was selected as a model protein to mimic the protein-rich environment in the blood. Compared with HMPBs, HMPBs@PEI-ZS and HMPBs@PEI-ZS-E5 exhibited low protein adsorption amounts after 1, 2, and 4 h incubation (Fig. 4a). This remarkably suppressed protein adsorption endowed the nanoparticles with good antifouling characteristics, which are beneficial for AML therapy.

It is known that the stability of nanocarriers is essential for better therapeutic effect. Size distribution of the nanocarrier after incubation in biological buffers can be used as an indicator to assess its stability. When suspended in PBS containing 10% FBS for 48 h, the size distribution of different HMPBs displays a narrow change, implying that these nanoparticles are aggregate-free and well-dispersed (Fig. 4b). The biocompatibilities of different HMPBs were further evaluated before the assessment of their therapeutic performances. We first confirmed that HMPBs in different formulations are biocompatible at concentrations as high as 100 μg mL^{-1} with cell viabilities above 90% (Fig. 4c). Consistently, no significant hemolysis was found in the presence of nanoparticles for 6 h (Fig. 4d). The results proved that these nanocarriers are biocompatible.

3.5 Intracellular uptake

Cellular uptake is critical for nanoparticles in the therapeutic process. Flow cytometry and CLSM were first employed to observe cellular uptake by HL60 cells. After being cultured with the free drug and different HMPBs, cells were collected to examine the cellular uptake efficiency. As shown in Fig. 5a, with the assistance of a nanocarrier, drugs could be transported

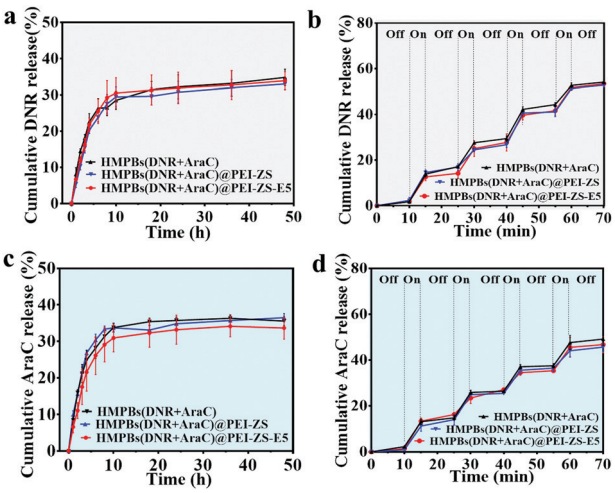

Fig. 3 The drug release profiles under physiologic conditions (a and c) without or (b and d) with laser irradiation.

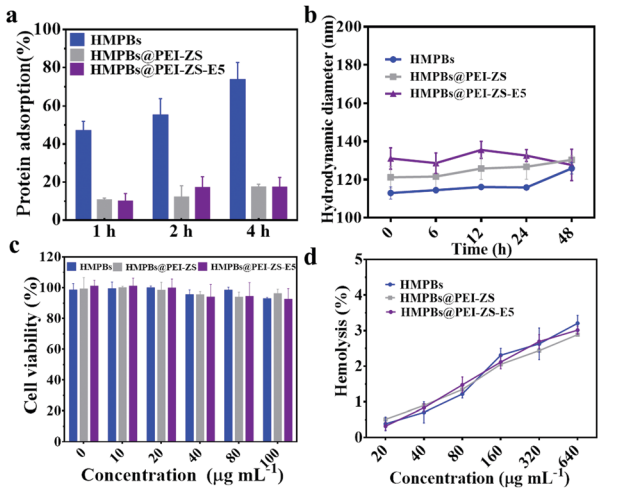

Fig. 4 (a) Protein adsorption of different HMPBs incubated with BSA for 1, 2, and 4 h. (b) Hydrodynamic size for different HMPBs measured by DLS. (c) Cytotoxicity of different HMPBs to HL60 cells, detected using CCK-8. (d) Hemolysis quantification of erythrocytes incubated with various concentrations of different HMPBs.

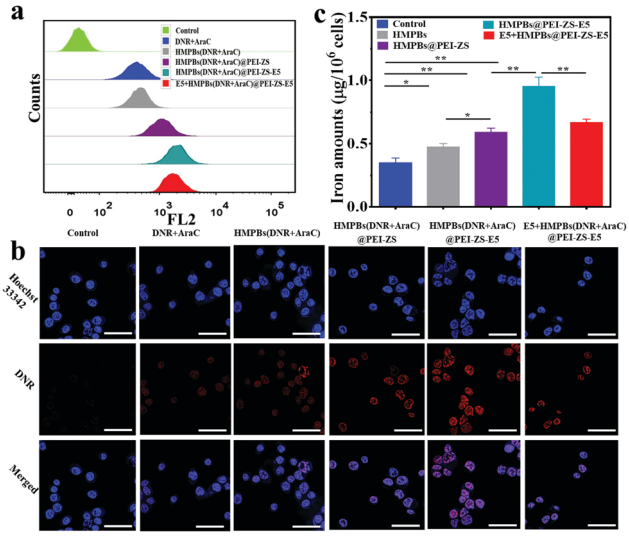

Fig. 5 Cellular uptake observations. (a) Cellular uptake detected by flow cytometry. (b) Fluorescence images of HL60 cells treated with free drug and different HMPBs for 4 h. The scale bar is 50 μm. (c) Fe contents of HL60 cells treated with different HMPBs for 24 h, as measured by ICP-OES. HL60 cells treated with E5 prior to incubation with nanoparticles. Data are given as mean ± SD (n = 3). *$p < 0.05$; **$p < 0.01$.

easily into HL60 cells. Clearly, the uptake by HL60 cells for HMPBs@PEI-ZS was superior to the level for HMPBs in terms of the fluorescence signals. The significant enhancement was most likely attributed to the positive surface charge of HMPBs@PEI-ZS, since it is easy for nanoparticles to bind to the negative cell membrane. Moreover, cells treated with HMPBs@PEI-ZS-E5 displayed stronger red fluorescence than those treated with HMPBs@PEI-ZS, suggesting the effective targeting efficiency of E5. Similar results were observed in the CLSM assay. Fluorescence images showed that the intracellular DNR fluorescence was mainly distributed in the nucleus (Fig. 5b), which is consistent with the reported literature.[50,51] This phenomenon further indicated that DNR could be successfully released from the nanocomposites to obtain access to the nucleus to exert a therapeutic effect, because only those that released DNR could enter the nucleus.

For the ICP assay, compared with HMPBs@PEI-ZS, HMPBs@PEI-ZS-E5 largely enhanced the cellular uptake efficiency by 1.6 times, and this means that the nanocarriers can perform selective drug delivery towards HL60 cells. Additionally, in the presence of E5, the uptake of HMPBs@PEI-ZS-E5 was significantly decreased by 30% (Fig. 5c). This phenomenon confirmed that the uptake of E5-ZS-PEI-HMPBs is mediated by CXCR4 receptor induced endocytosis.

3.6 Targeted and synergetic chemo-photothermal promoted cell apoptosis

For the synergistic effect of nanoplatforms on AML targeting and chemo-photothermal therapy *in vitro*, a CCK-8 assay was first used to evaluate the cell viabilities after treatment with different nanoagents under different conditions. As shown in Fig. 6a, all of the therapies showed an increasing inhibition rate against HL60 cells in a dose-dependent manner. It is clear that about 34.6% of HL60 cells incubated with 50 μg mL^{-1} of HMPBs(DNR + AraC)@PEI-ZS were viable, however, the survival of the cells cultured with HMPBs(DNR + AraC)@PEI-ZS-E5 was 22.2%. The cell viability of the HMPBs(DNR + AraC)@PEI-ZS-E5 + Laser group was less than that of the HMPBs@PEI-ZS-E5 + Laser group and than that of the HMPBs(DNR + AraC)@PEI-ZS-E5 group. HL60 cells treated with the highest dosage of HMPBs(DNR + AraC)@PEI-ZS-E5 under laser exposure possessed the lowest survival rate (8.68%). The superior treatment was mainly attributed to the following factors. Firstly, the targeting specificity of the nanoagent played an important role. Secondly, the laser irradiation can not only guide photothermal therapy, but also elevate the drug release from the nanoagent to kill the HL60 cells.

Annexin V-APC/7-AAD staining was applied to identify apoptosis induced by the targeted chemo-photothermal treatment. Few apoptotic cells were observed when exposed to the laser alone, indicating that the power density and the exposure time were safe for the HL60 cells. As expected, the HMPBs(DNR + AraC)@PEI-ZS-E5 + Laser group showed a remarkable increase in apoptotic cells compared to the other groups, confirming the data obtained in the CCK-8 assay (Fig. 6b).

We further conducted a calcein-AM/PI co-staining assay to visualize the targeted and chemo-photothermal effect of the nanoagent by staining live/dead cells. Compared to the HMPBs(DNR + AraC)@PEI-ZS-E5 group and the HMPBs@PEI-ZS-E5 + Laser group, the HL60 cells showed the lowest density of green fluorescence (live cells) and the highest density of red fluorescence (dead cells) when treated with HMPBs(DNR + AraC)@PEI-ZS-E5 under laser irradiation (Fig. 6c). The results successfully demonstrated that HMPBs(DNR + AraC)@PEI-ZS-E5

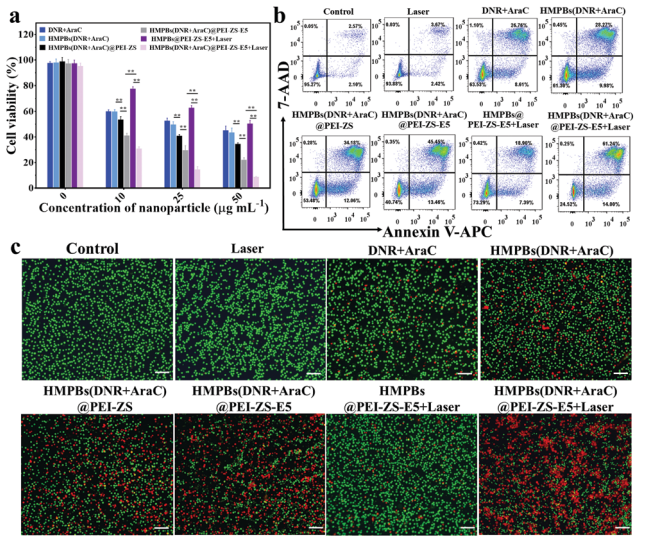

Fig. 6 *In vitro* targeted and synergetic chemo-photothermal effects. (a) Cell viabilities of HL60 cells after various treatments, determined by CCK-8 assay. (b) Apoptosis of HL60 cells detected by flow cytometry. (c) Fluorescence images of calcein-AM/PI co-stained HL60 cells after various treatments. The scale bar is 100 μm.

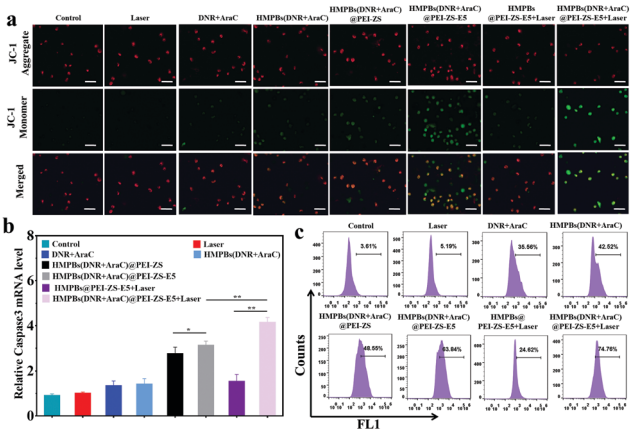

Fig. 7 (a) Fluorescence microscopy images of HL60 cells stained by JC-1. (b) Detection of Caspase3 expression levels by qRT-PCR. (c) Detection of H2AX levels using flow cytometry. HL60 cells were treated with different HMPBs with or without laser irradiation. The scale bar is 50 μm.

combined with laser irradiation could achieve the most effective inhibitory effect of the HL60 cells.

Many important events in the process of cell apoptosis are closely associated with mitochondria, including the release of the caspase activator, the change in electron transport chain, the damage of MMP, *etc.*[52] To investigate whether the mitochondria is dysfunctional after treatment, we used JC-1 to evaluate the apoptosis of HL60 cells with various treatments. JC-1 molecules form aggregates in normal mitochondria and exist as monomers in damaged mitochondria, which emit red and green fluorescence, respectively. Stronger green fluorescence was observed in the HL60 cells treated with HMPBs(DNR + AraC)@PEI-ZS-E5 under laser irradiation compared to either the non-targeted or therapies alone group, suggesting a considerably higher level of apoptosis, further confirming the targeting and synergetic chemo-photothermal treatment of AML (Fig. 7a). In general, the activation of Caspase3 is a key event in cell apoptosis, and is regarded as a reliable indicator of apoptosis.[53] The highest Caspase3 mRNA expression levels of the cells treated with HMPBs(DNR + AraC)@PEI-ZS-E5 with laser irradiation strongly support the CXCR4 targeting efficacy and the chemo-thermotherapy synergetic effect (Fig. 7b). The phosphorylation of H2AX is considered to be an indicator of DNA double-strand breakage. As shown in Fig. 7c, the cells in the HMPBs(DNR + AraC)@PEI-ZS-E5 + Laser group showed significantly higher H2AX levels than the cells in either the HMPBs(DNR + AraC)@PEI-ZS-E5 or HMPBs@PEI-ZS-E5 + Laser groups, indicating severe DNA damage in the synergetic chemo-photothermal group. In addition, we found that the hyperthermia group showed elevated ROS levels in HL60 cells (Fig. S6, ESI†), confirming that hyperthermia causes DNA damage indirectly by producing ROS.[54] On the other hand, the presence of DNR released from nanoparticles also induces DNA double-strand breaks.[55] Taken together, and compared to the results of either therapies alone, the combinatorial treatment seems to be very effective in decreasing MMP, increasing Caspase3 expression, inducing DNA damage and consequently causing cell death.

4. Conclusions

In this work, a novel nanoagent of HMPBs(DNR + AraC)@PEI-ZS-E5 was fabricated to combine multiple functions into a nanocarrier for active-targeting, laser-induced drug release, and chemo-photothermal therapy to treat AML *in vitro*. The nanoplatform possessed excellent photothermal performance, a protein antifouling property, photothermal stability and satisfactory biocompatibility. The HMPBs(DNR + AraC)@PEI-ZS-E5 + Laser group is more effective in disrupting MMP, activating Caspase3, inducing DNA damage and killing HL60 cells, suggesting the use of a combined effect of targeting/chemo/photothermal treatment of AML *in vitro*. Hyperthermia for AML treatment *in vivo* has a number of challenges, such as the blood dilution effects of nanoparticles and the selection of a safe laser power intensity. Since Prussian blue has been approved by the FDA for use in the clinic, compared with other photothermal reagents, Prussian blue is more likely to be used in large doses to counteract the blood-thinning effect. The best power density to use in animal models or for use in humans in the future should not only achieve the better chemo-photothermal effect, but it should also not harm healthy tissue. Hence, tremendous efforts and explorations are needed to advance the *in vivo* applications.

Consequently, the development of nanoparticles has brought many possibilities for the advancement of nanomedicine, especially in imaging, molecular diagnosis and targeted therapy. However, the era of nanomedicine is still in its infancy, and the rational design, large-scale prepration, quality controls and synthetic costs should be taken into account to improve the engineering of future nanotherapeutics. Since extensive preclinical knowledge and clinical expertise is being accumulated, it is quite likely that nanomedicines will rapidly emerge in diagnostic and therapeutic fields. It is also believed that nanoparticles will certainly occupy an important place in clinical applications.

Conflicts of interest

The authors declare no conflicts of interest.

Acknowledgements

This research was supported by the National Key Research and Development Program of China (No. 2017YFA0205502), the National Natural Science Foundation of China (No. 61821002, 82072067 and 81972555), the Science and Technology Support Project of Jiangsu Province (No. BE2017763), the Medical Research Project of Jiangsu Province Health Committee (No. K2019020) and the Fundamental Research Funds for the Central Universities.

Notes and references

1 S. J. Busfield, M. Biondo, M. Wong, H. S. Ramshaw, E. M. Lee, S. Ghosh, H. Braley, C. Panousis, A. W. Roberts,

S. Z. He, D. Thomas, L. Fabri, G. Vairo, R. B. Lock, A. F. Lopez and A. D. Nash, *Leukemia*, 2014, **28**, 2213–2221.
2 E. A. Griffiths, H. E. Carraway, N. S. Chandhok and T. Prebet, *Leuk. Res.*, 2020, **91**, 106339.
3 H. Dombret and C. Gardin, *Blood*, 2016, **127**, 53–61.
4 A. K. Iyer, A. Singh, S. Ganta and M. M. Amiji, *Adv. Drug Delivery Rev.*, 2013, **65**, 1784–1802.
5 G. Montalban-Bravo and G. Garcia-Manero, *Leukemia*, 2015, **29**, 760–769.
6 F. Greco and M. J. Vicent, *Adv. Drug Delivery Rev.*, 2009, **61**, 1203–1213.
7 J. Li, F. Zhang, Z. Hu, W. Song, G. Li, G. Liang, J. Zhou, K. Li, Y. Cao, Z. Luo and K. Cai, *Adv. Healthcare Mater.*, 2017, **6**, 1700005.
8 W. Chen, K. Zeng, H. Liu, J. Ouyang, L. Wang, Y. Liu, H. Wang, L. Deng and Y.-N. Liu, *Adv. Funct. Mater.*, 2017, **27**, 1605795.
9 L. Cheng, F. Zhang, S. Wang, X. Pan, S. Han, S. Liu, J. Ma, H. Wang, H. Shen, H. Liu and Q. Yuan, *Angew. Chem., Int. Ed.*, 2019, **58**, 7728–7732.
10 A. Bansal and Y. Zhang, *Acc. Chem. Res.*, 2014, **47**, 3052–3060.
11 A. M. Alkilany, L. B. Thompson, S. P. Boulos, P. N. Sisco and C. J. Murphy, *Adv. Drug Delivery Rev.*, 2012, **64**, 190–199.
12 H. Zhang, Y. Pei, X. Zhang, L. Zhu, L. Hou, J. Chang and Z. Zhang, *Appl. Mater. Today*, 2020, **18**, 100494.
13 X. Huang, R. Gu, J. Li, N. Yang, Z. Cheng, W. Si, P. Chen, W. Huang and X. Dong, *Sci. China: Chem.*, 2019, **63**, 55–64.
14 L. Cheng, C. Wang, L. Feng, K. Yang and Z. Liu, *Chem. Rev.*, 2014, **114**, 10869–10939.
15 Y. Zhang, L. Huang, Z. Li, G. Ma, Y. Zhou and G. Han, *ACS Nano*, 2016, **10**, 3881–3885.
16 Z. Zhang, L. Wang, J. Wang, X. Jiang, X. Li, Z. Hu, Y. Ji, X. Wu and C. Chen, *Adv. Mater.*, 2012, **24**, 1418–1423.
17 H. Liu, T. Liu, X. Wu, L. Li, L. Tan, D. Chen and F. Tang, *Adv. Mater.*, 2012, **24**, 755–761.
18 Q. Tian, M. Tang, Y. Sun, R. Zou, Z. Chen, M. Zhu, S. Yang, J. Wang, J. Wang and J. Hu, *Adv. Mater.*, 2011, **23**, 3542–3547.
19 K. Yang, L. Hu, X. Ma, S. Ye, L. Cheng, X. Shi, C. Li, Y. Li and Z. Liu, *Adv. Mater.*, 2012, **24**, 1868–1872.
20 J. Yang, J. Choi, D. Bang, E. Kim, E. K. Lim, H. Park, J. S. Suh, K. Lee, K. H. Yoo, E. K. Kim, Y. M. Huh and S. Haam, *Angew. Chem., Int. Ed.*, 2011, **50**, 441–444.
21 C. Tong, X. Zhang, J. Fan, B. Li, B. Liu, M. Daniyal and W. Wang, *Sci. Bull.*, 2018, **63**, 935–946.
22 L. Cheng, H. Gong, W. Zhu, J. Liu, X. Wang, G. Liu and Z. Liu, *Biomaterials*, 2014, **35**, 9844–9852.
23 X. Cai, X. Jia, W. Gao, K. Zhang, M. Ma, S. Wang, Y. Zheng, J. Shi and H. Chen, *Adv. Funct. Mater.*, 2015, **25**, 2520–2529.
24 L. Jing, S. Shao, Y. Wang, Y. Yang, X. Yue and Z. Dai, *Theranostics*, 2016, **6**, 40–53.
25 W. Zhang, S. Hu, J. J. Yin, W. He, W. Lu, M. Ma, N. Gu and Y. Zhang, *J. Am. Chem. Soc.*, 2016, **138**, 5860–5865.
26 H. Y. Lian, M. Hu, C. H. Liu, Y. Yamauchi and K. C. Wu, *Chem. Commun.*, 2012, **48**, 5151–5153.
27 X. Liang, Z. Deng, L. Jing, X. Li, Z. Dai, C. Li and M. Huang, *Chem. Commun.*, 2013, **49**, 11029.
28 J. Ma, K. Kang, Y. Zhang, Q. Yi and Z. Gu, *ACS Appl. Mater. Interfaces*, 2018, **10**, 43923–43935.
29 J. B. Schlenoff, *Langmuir*, 2014, **30**, 9625–9636.
30 Y. Zhu, J. Wang, F. Zhang, S. Gao, A. Wang, W. Fang and J. Jin, *Adv. Funct. Mater.*, 2018, **28**, 1804121.
31 S. Shi, Y. Huang, X. Chen, J. Weng and N. Zheng, *ACS Appl. Mater. Interfaces*, 2015, **7**, 14369–14375.
32 K. Y. Choi, S. Correa, J. Min, J. Li, S. Roy, K. H. Laccetti, E. Dreaden, S. Kong, R. Heo, Y. H. Roh, E. C. Lawson, P. A. Palmer and P. T. Hammond, *Adv. Funct. Mater.*, 2019, **29**, 1900018.
33 Z. Wang, Y. Ma, X. Yu, Q. Niu, Z. Han, H. Wang, T. Li, D. Fu, S. Achilefu, Z. Qian and Y. Gu, *Adv. Funct. Mater.*, 2018, **28**, 1800732.
34 X. Fang, H. Xie, H. Duan, P. Li, M. Yousaf, H. Xu, Y. Yang and C. Wang, *PLoS One*, 2017, **12**, e0182697.
35 J. Guo, X. Luan, Z. Cong, Y. Sun, L. Wang, S. L. McKenna, M. R. Cahill and C. M. O'Driscoll, *J. Controlled Release*, 2018, **286**, 154–166.
36 R. Deng, N. Shen, Y. Yang, H. Yu, S. Xu, Y. W. Yang, S. Liu, K. Meguellati and F. Yan, *Biomaterials*, 2018, **167**, 80–90.
37 J. Meng, Y. Ge, H. Xing, H. Wei, S. Xu, J. Liu, D. Yan, T. Wen, M. Wang, X. Fang, L. Ma, Y. Yang, C. Wang, J. Wang and H. Xu, *Small*, 2020, **16**, e2001890.
38 R. Zu, X. Fang, Y. Lin, S. Xu, J. Meng, H. Xu, Y. Yang and C. Wang, *J. Biomater. Sci., Polym. Ed.*, 2020, **31**, 1604–1621.
39 X. Li, H. Guo, H. Duan, Y. Yang, J. Meng, J. Liu, C. Wang and H. Xu, *Sci. Rep.*, 2015, **5**, 16228.
40 X. Li, H. Guo, Y. Yang, J. Meng, J. Liu, C. Wang and H. Xu, *Sci. Rep.*, 2014, **4**, 6610.
41 R. Zu, X. Fang, Y. Lin, S. Xu, J. Meng, H. Xu, Y. Yang and C. Wang, *J. Biomater. Sci., Polym. Ed.*, 2020, **31**, 1604–1621.
42 J. Meng, Y. Ge, H. Xing, H. Wei, S. Xu, J. Liu, D. Yan, T. Wen, M. Wang, X. Fang, L. Ma, Y. Yang, C. Wang, J. Wang and H. Xu, *Small*, 2020, **16**, 2001890.
43 Z. Zhou, L. Wang, X. Chi, J. Bao, L. Yang, W. Zhao, Z. Chen, X. Wang, X. Chen and J. Gao, *ACS Nano*, 2013, **7**, 3287–3296.
44 S. Muthusamy, J. Charles, B. Renganathan and D. Sastikumar, *J. Mater. Sci.*, 2018, **53**, 15401–15417.
45 D. Pentak, M. Maciazek-Jurczyk and Z. H. Zawada, *Sci. Eng. C Mater. Biol. Appl*, 2017, **73**, 388–397.
46 D. Pentak and M. Maciążek-Jurczyk, *J. Mol. Liq.*, 2019, **278**, 115–123.
47 R. K. Thapa, S. K. Ku, H. G. Choi, C. S. Yong, J. H. Byeon and J. O. Kim, *Nanoscale*, 2018, **10**, 1742–1749.
48 R. Mehmood, S. S. Mofarah, A. Rawal, F. Tomasetig, X. Wang, J.-L. Yang, P. Koshy and C. C. Sorrell, *ACS Sustainable Chem. Eng.*, 2019, **7**, 9189–9201.
49 H. Wei, N. Insin, J. Lee, H. S. Han, J. M. Cordero, W. Liu and M. G. Bawendi, *Nano Lett.*, 2012, **12**, 22–25.
50 D. Yan, H. Wei, X. Lai, Y. Ge, S. Xu, J. Meng, T. Wen, J. Liu, W. Zhang, J. Wang and H. Xu, *J. Controlled Release*, 2020, **327**, 766–778.
51 X. Lin, Y. Cao, J. Li, D. Zheng, S. Lan, Y. Xue, F. Yu, M. Wu and X. Zhu, *Biomater. Sci.*, 2019, **7**, 2996–3006.

52 H. Y. Long, Q. X. Huang, Y. Y. Yu, Z. B. Zhang, Z. W. Yao, H. B. Chen and J. W. Feng, *Arch. Med. Sci.*, 2019, **15**, 765–773.
53 Y.-J. Lu, E.-Y. Chuang, Y.-H. Cheng, T. S. Anilkumar, H.-A. Chen and J.-P. Chen, *Chem. Eng. J.*, 2019, **373**, 720–733.
54 M. Dabaghi, R. Quaas and I. Hilger, *Cancers*, 2020, **12**, 2562.
55 H. M. Al-Aamri, H. Ku, H. R. Irving, J. Tucci, T. Meehan-Andrews and C. Bradley, *BMC Cancer*, 2019, **19**, 179.